Title
Single Quasi-1D Chains of Sb2Se3 Encapsulated within Carbon Nanotubes.

Journal
Chemistry of Materials, 36(2)

ISSN
0897-4756

Authors
Milligan, Griffin
Yao, Ze-Fan
Cordova, Dmitri
et al.

Publication Date
2024-01-23

DOI
10.1021/acs.chemmater.3c02114

Peer reviewed

CHEMISTRY OF MATERIALS

pubs.acs.org/cm
Article

Single Quasi-1D Chains of Sb_2Se_3 Encapsulated within Carbon Nanotubes

Griffin M. Milligan, Ze-Fan Yao, Dmitri Leo Mesoza Cordova, Baixin Tong, and Maxx Q. Arguilla*

Cite This: *Chem. Mater.* 2024, 36, 730−741
Read Online

ABSTRACT: The realization of stable monolayers from 2D van der Waals (vdW) solids has fueled the search for exfoliable crystals with even lower dimensionalities. To this end, 1D and quasi-1D (q-1D) vdW crystals comprising weakly bound subnanometer-thick chains have been discovered and demonstrated to exhibit nascent physics in the bulk. Although established micromechanical and liquid-phase exfoliation methods have been applied to access single isolated chains from bulk crystals, interchain vdW interactions with nonequivalent strengths have greatly hindered the ability to achieve uniform single isolated chains. Here, we report that encapsulation of the model q-1D vdW crystal, Sb_2Se_3, within single-walled carbon nanotubes (CNTs) circumvents the relatively stronger *c*-axis vdW interactions between the chains and allows for the isolation of single chains with structural integrity. High-resolution transmission electron microscopy and selected area electron diffraction studies of the Sb_2Se_3@CNT heterostructure revealed that the structure of the $[Sb_4Se_6]_n$ chain is preserved, enabling us to systematically probe the size-dependent properties of Sb_2Se_3 from the bulk down to a single chain. We show that ensembles of the $[Sb_4Se_6]_n$ chains within CNTs display Raman confinement effects and an emergent band-like absorption onset around 600 nm, suggesting a strong blue shift of the near-infrared band gap of Sb_2Se_3 into the visible range upon encapsulation. First-principles density functional theory calculations further provided qualitative insight into the structures and interactions that could manifest in the Sb_2Se_3@CNT heterostructure. Spatial visualization of the calculated electron density difference map of the heterostructure indicated a minimal degree of electron donation from the host CNT to the guest $[Sb_4Se_6]_n$ chain. Altogether, this model system demonstrates that 1D and q-1D vdW crystals with strongly anisotropic vdW interactions can be precisely studied by encapsulation within CNTs with suitable diameters, thereby opening opportunities in understanding dimension-dependent properties of a plethora of emergent vdW solids at or approaching the subnanometer regime.

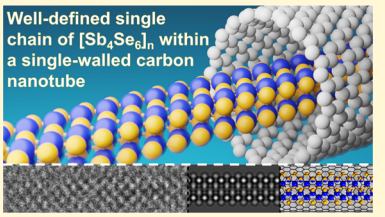

1. INTRODUCTION

The discovery of solids that exhibit unusual physics and unexpected behaviors at or approaching the atomic scale has, for the longest time, consistently relied on ideal conditions, often requiring inert chemical environments or stable surface passivation.[1−4] Remarkably, the advent of 2D van der Waals (vdW) solids has changed the way in which ultrathin solids are accessed.[5−8] By hosting atomically precise layers held together by weak vdW interactions, stable solids with sizable lateral dimensions which approach single-atom thicknesses can be accessed from either top-down exfoliation or bottom-up vapor growth.[7,9] This new materials paradigm has facilitated not only the realization of exotic physics in engineered multilayers and at the monolayer limit but has also inspired the search toward solid-state structures with even lower dimensionalities[8,10−20]

Most recently, there has been a growing interest in the creation and rediscovery of crystals with even lower dimensions and comprising vdW-bound one-dimensional (1D) or quasi-1D (q-1D) chains with subnanometer cross-sections.[21−27] Owing to the 1D character of these crystals, emergent properties such as higher-order topological states,[2,26,28] Dirac polarons,[29] controllable charge density waves,[25] high-fidelity electron transport,[22] excitonic insulating states,[30] and even unconventional superconductivity[31,32] have been demonstrated. Furthermore, the vdW nature of these 1D and q-1D vdW crystals has allowed for the implementation of top-down exfoliation routes previously established for 2D vdW crystals to access ultrathin nanostructures approaching sub-10 nm thicknesses.[27,33−36] While these strategies have been successful, controlling the size distribution and morphology of the resulting nanostructures remains a challenge and often results in a combination of nanowires, nanoribbons, or nanosheets. This diverse distribution of the nanostructures can be rationalized in terms of the unique vdW cleavage directions in the basal plane (plane perpendicular to the long chain axis) of the 1D and q-1D vdW crystals. While equivalent between adjacent sheets in 2D vdW crystals like graphene, the strength of vdW interactions in 1D and q-1D vdW crystals is strongly dependent on the orientation and cross-sectional profile of the constituent chains.[35,37−39] These nonequivalent

Received: August 21, 2023
Revised: December 27, 2023
Accepted: December 28, 2023
Published: January 11, 2024

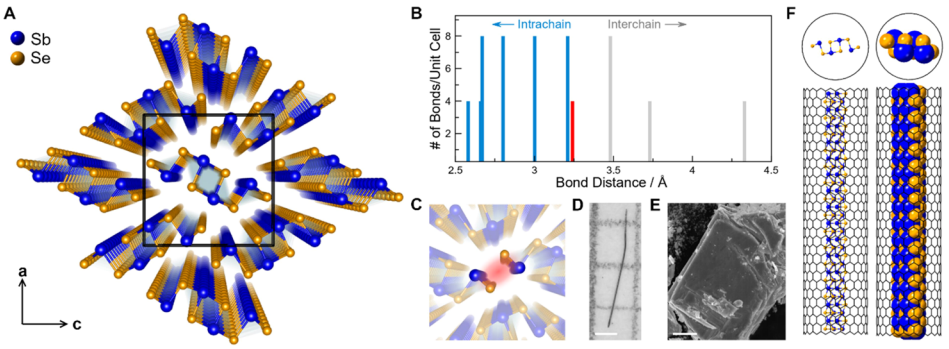

Figure 1. Quasi-1D vdW structure of Sb_2Se_3 and proposed encapsulation of a $[Sb_4Se_6]_n$ single chain within CNT. (A) Crystal structure representation of Sb_2Se_3 oriented along the covalent *b*-axis ([010] zone direction).[40] The unit cell is shown as a black box. Sb atoms are represented in blue, and Se atoms are represented in orange. Graphical (B) and crystal structure representations (C) of the anisotropic bonding interactions that contribute to the formation of quasi-2D nanoscale morphologies. The plot in B highlights the bond distances within (intrachain) and across (interchain) the $[Sb_4Se_6]_n$ chains. The shortest interchain interaction is highlighted in red for both atoms B and C. (D) Optical micrograph of a sizable bulk Sb_2Se_3 single crystal showing a 1D needle-like crystalline habit. Scale bar: 0.5 mm. (E) SEM image of a micromechanically cleaved Sb_2Se_3 crystal showing a 2D plate-like morphology. Scale bar: 5 μm. (F) Proposed structural representation of the heterostructure of a (21,0) CNT filled with a single Sb_2Se_3 covalent chain, Sb_2Se_3@CNT. Sb_2Se_3 is shown as either a ball and stick (left) or space-filling (right) structure, while CNTs are shown as wireframe structures for clarity.

interchain interactions ultimately obscure the isolation of single chains from these vdW crystals.[35,37−39]

The apparent anisotropy in the interchain vdW interactions in 1D and q-1D vdW phases is most pronounced in the class of pnictogen chalcogenides (Pn_2Ch_3; Pn = Sb, Bi; Ch = S, Se) (Figure 1A).[33,36,37,40−43] These crystals, with the exception of Bi_2Se_3 which crystallizes in 2D, are composed of q-1D $[Pn_4Ch_6]_n$ chains stacked together to form an orthorhombic lattice. As a model pnictogen chalcogenide phase, Sb_2Se_3 has gained attention due to its anisotropic q-1D nature, intrinsic band gap reported to be in the 1−1.2 eV range, and high visible-to-near-infrared absorption coefficient greater than 10^5 cm^{-1}, each of which is ideal for applications in thin film photovoltaic devices, directional near-infrared (NIR) photodetectors, and nonvolatile phase change photonic devices.[35,40,44−48] These attributes have made Sb_2Se_3 an attractive building block in next-generation photovoltaics, where it has been demonstrated to approach the 10% efficiency benchmark and to host minimal carrier recombination rates due to its benign grain boundaries arising from interchain vdW interactions.[44,45,48,49] Beyond the bulk and thin film form, predictions suggesting that exfoliation into a single covalent chain induces an elusive indirect-to-direct gap transition in pnictogen chalcogenides have led to significant effort toward exfoliation of Sb_2Se_3 and related phases.[37,42,43] These studies, which employed established top-down exfoliation approaches, resulted in nanostructures that consistently displayed quasi-2D sheet-like behavior: nanoribbons and nanosheets each with various lateral sizes and thicknesses.

The observation of quasi-2D nanostructures is consistent with previous exfoliation reports on other 1D and q-1D vdW phases.[33,35,36,39,50] Specifically, for Sb_2Se_3, the formation of quasi-2D nanostructures is corroborated by experimental single crystal structure analyses and first-principles DFT calculations on the bulk structure.[37,38,51] These reports consistently describe the significantly stronger interchain interaction between the $[Sb_4Se_6]_n$ chains in Sb_2Se_3 along the *c*-axis ([001]) direction. From photoelectron spectroscopy and DFT,[37,40] it was shown that the significant interchain interaction along the [001] direction stems from the interaction between the antibonding *s* states of the stereochemically active Sb lone pairs with the electronegative p states of Se in the neighboring chain.[38] To visually illustrate this, we show the bond length distribution between the Sb and Se atoms in the orthorhombic Sb_2Se_3 structure (Figure 1B). By separating the intrachain (in blue) and vdW interchain (in gray) interactions, we note that the bonding interactions across the chains in the *c*-axis ([001]) direction (in red) is significantly shorter (3.247 Å) than the rest of the nearest-neighbor interchain Sb−Se distances (3.486 and 3.739 Å).[40] This interaction is graphically highlighted in the close-up crystal structure of Sb_2Se_3 (Figure 1C). The influence of these anisotropic interchain interactions is also evident in the lab-grown needle-like crystalline habit of cm-long Sb_2Se_3 single crystals (Figure 1D) which, when micromechanically exfoliated, expose nanosheet-like cleavage planes in SEM imaging (Figure 1E). Therefore, alternative strategies are warranted to overcome these intrinsic bonding limitations that hinder the top-down exfoliation of 1D and q-1D crystals down to the single chain.

To overcome the limitations brought about by the strong interchain interactions arising from the stereochemically active 5s lone pairs of Sb, we sought alternative routes to precisely access isolated chains of Sb_2Se_3. To this end, encapsulation routes within nanotubes such as single or multiwalled carbon nanotubes (CNTs) or boron nitride nanotubes have been employed to isolate well-defined, precise nanowires (Figure 1F). This strategy has been demonstrated to harbor metastable 1D phases that would not exist without the stabilization of the nanotube with many competing phases.[52−66] Throughout this article, these heterostructures will be denoted as "*material@CNT*" by convention. This system allows for long-range order and atomic precision of the guest structures within the host nanotubes due to the inert vdW surface of CNTs which would be the ideal conditions to isolate the single chains of 1D and q-1D vdW crystals to form vdW−vdW interfaces. Encouragingly, encapsulation within CNTs has also been used to isolate 1D vdW transition metal trichalcogenides (TMTs) with weak interchain vdW interactions such as $NbSe_3$ and $HfTe_3$ into single covalent chains and to stabilize novel TMT metastable phases not accessible through the bulk phase such as $NbTe_3$, VTe_3, and $TiTe_3$.[53,54] A key enabling factor in stabilizing these

https://doi.org/10.1021/acs.chemmater.3c02114
Chem. Mater. 2024, 36, 730−741

structures is the inert vdW environment within the CNT host, which protects the guest structures from ambient air- or chemically induced degradation. As such, encapsulation within CNTs has also been used to access the formation of atomically precise nanoribbon-like monolayer structures, zigzag strips, and even helical chains derived from 2D vdW crystals by protecting the in-plane dangling bonds from oxidation in ambient conditions.[56,58,60,67] Enabled by the atomic precision of the guest structures inside CNTs, these heterostructures have been used as a reliable platform to investigate the evolution of the photophysics,[57,58] electron transport,[65] magnetic interactions,[68] and electron−phonon coupling[56] upon encapsulation of a library of guest structures.[19,56,68] We aimed to employ this synthetic strategy to isolate single chains of our model q-1D vdW phase, Sb_2Se_3, and use the resulting heterostructure to probe the evolution of the structural attributes and photophysical properties of Sb_2Se_3 upon encapsulation.

Here, we report the encapsulation of a single chain of a model q-1D vdW phase, Sb_2Se_3, within a single-walled CNT. By using a suitable CNT with an average 1.6 ± 0.4 nm inner diameter, we found that matching the CNT's internal diameter to a size slightly larger than the cross-sectional dimension of a single Sb_2Se_3 chain preserves the structural integrity of a single chain upon encapsulation and effectively suppresses the strong interchain interactions arising from the polarization of the stereochemically active 5s lone pairs of Sb by the adjacent 4p orbitals of Se. We further show the direct consequence of confinement on the Raman-active modes and optical properties of encapsulated $[Sb_4Se_6]_n$ single chains as well as the influence of the guest chains on the structure of the CNT. Among these results, we highlight the emergence of a significant visible range absorption band in the absorption spectra of Sb_2Se_3@CNT, which indicates a significant confinement-induced blue shift of the band gap of Sb_2Se_3 upon encapsulation. Our results underscore the potential of nanoscale growth within CNTs to encapsulate functional 1D and q-1D structures that display strong anisotropic interchain interactions that traditional top-down routes could not effectively overcome.

2. EXPERIMENTAL SECTION

2.1. General Methods for Data and Crystal Structure Plotting. Crystal structure representations were generated in *SingleCrystal 4* software (CrystalMaker Software Suite). The nanotube models were generated in either *SingleCrystal 4* or *Avogadro*: an open-source molecular builder and visualization tool (Version 1.2.0. http://avogadro.cc/).[69] The bond distance plot featured in Figure 1b was generated in *VESTA*[70] using the experimental crystal structure of Sb_2Se_3. All figures were finished and were compiled using *Lunacy*.

2.2. Synthesis of Bulk Sb_2Se_3 Precursors. Elemental precursors of antimony (99.5%) and selenium (99.5%) were purchased from STREM and used without further purification. Bulk Sb_2Se_3 crystals that were used as precursors for subsequent syntheses were grown as follows: Stoichiometric quantities of Sb and Se (2:3 ratio) were evacuated in quartz ampules (10 mm inner diameter, I.D.; 12 mm outer diameter, O.D.) under a <100 mTorr base pressure and were subsequently flame-sealed. The ampules were then uniformly heated to 800 °C for 96 h in either a muffle furnace (KSL-1200X; MTI Inc.) or a single-zone vertical tube furnace (OTF-1200F; MTI Inc.) then cooled over the course of 48 h. Single crystals were mechanically isolated from the melt and were imaged via optical microscopy. The phase purity of the Sb_2Se_3 polycrystals was confirmed by powder X-ray diffraction on a Rigaku MiniFlex diffractometer. The resulting diffractogram was compared to the reported literature structure.[40] Beyond the polycrystalline melt obtained postsynthesis, long single crystals of Sb_2Se_3 were also collected from the walls of the ampule. While relatively air-stable, the resulting bulk crystals of Sb_2Se_3 were kept in a vacuum desiccator prior to encapsulation within SWCNTs to prevent any deposition of material from ambient air.

2.3. Encapsulation of Sb_2Se_3 within SWCNTs. High-purity CNTs (1.6 ± 0.4 nm diameter, Tuball, OCSiAl) were pretreated by heating the as-received nanotubes at 420 °C in ambient air conditions for 5 h. This step selectively oxidizes and opens both ends of the CNTs and was found to be crucial for the subsequent encapsulation of Sb_2Se_3.[63] Approximately 10 mg of these pretreated CNTs were then loaded into quartz ampules immediately after heat treatment (10 mm I.D.; 12 mm O.D.) and mixed with a large excess of powdered Sb_2Se_3 polycrystals, ranging from 200 to 300 mg. Ampules containing the CNTs and Sb_2Se_3 powders were evacuated under vacuum with an approximately <100 mTorr base pressure and were immediately flame-sealed. The ampules were then heated to 800 °C for 96 h in either a muffle furnace (KSL-1200X; MTI Inc.) or a single-zone vertical tube furnace (OTF-1200F; MTI Inc.) then cooled over the course of 48 h. After the reaction, the Sb_2Se_3@CNTs were found to have been phase separated from the Sb_2Se_3 melt. The phase-pure Sb_2Se_3@CNTs that readily sits on top of the solidified melt were physically isolated from the resulting bulk Sb_2Se_3 boule and were used in the succeeding experiments without any further purification.

2.4. High-Resolution Transmission Electron Microscopy (HRTEM), Selected-Area Electron Diffraction (SAED), Scanning Transmission Electron Microscopy (STEM), and Elemental Mapping. The resulting Sb_2Se_3@CNT heterostructures and empty CNTs were dispersed in isopropanol (*i*-PrOH, 99.8%, Fisher Scientific) by bath sonication for 1 h and were drop-casted onto lacey carbon grids (Lacey Formvar/Carbon, 200 mesh, Cu grid; Ted Pella, Inc.). After being allowed to air-dry for 10 min, the grids bearing the Sb_2Se_3@CNT heterostructures or empty CNTs were stored in a vacuum desiccator overnight prior to measurement. Similarly, crystals of Sb_2Se_3 were solution exfoliated via bath sonication in *i*-PrOH for 2 h. The *i*-PrOH suspension with the exfoliated Sb_2Se_3 nanocrystallites was then drop-cast onto lacey carbon grids. HRTEM images and SAED patterns were acquired using a JEOL JEM-2800 S/TEM operated at an accelerating voltage of 200 kV. The electron microscope is equipped with a Schottky-type field emission electron source, SAED capabilities, and a Gatan OneView 4K camera with drift correction. Bright- and annular dark-field aberration-corrected STEM images and energy-dispersive X-ray spectra (EDS) of Sb_2Se_3@CNTs were collected by using a JEOL JEM-ARM300F Grand Arm electron microscope operated at either 80 or 300 kV acceleration voltage. Postprocessing and image analyses of raw HRTEM and STEM data (.dm4) were done using Gatan DigitalMicrograph software. Fast Fourier transform (FFT) analyses of the micrographs were done using ImageJ. Indexing of the SAED and FFT data were performed by comparing the experimental patterns with simulated patterns of the bulk single crystal structure using the *SingleCrystal 4* software (CrystalMaker Software Suite). HRTEM images were simulated using the *clTEM* software[71] from a .xyz file of single chain Sb_2Se_3 generated in VESTA by extending the unit cell along the *b*-axis, then manually excluding any atoms that are not covalently bound to the single chain.

2.5. Scanning Electron Microscopy (SEM) and Compositional Analysis Using EDS. Samples that were used for SEM imaging were prepared by embedding the fibrous ensembles and microcrystallites of the samples (Sb_2Se_3@CNTs, CNTs, or Sb_2Se_3) onto carbon tape secured onto aluminum SEM stubs. The samples were evenly distributed and flattened using a spatula to ensure conductive contact with the carbon tape and stub. SEM imaging and EDS analyses were performed using an FEI Quanta 3D FEG Dual Beam SEM, equipped with an Oxford silicon drift EDS detector operated using the INCA software. SEM Imaging and EDS analyses were performed at an operating voltage of 20 kV and a beam current of at least 1 nA.

2.6. X-ray Photoelectron Spectroscopy (XPS). XPS measurements of Sb_2Se_3@CNTs, CNTs, and bulk Sb_2Se_3 crystallites were

https://doi.org/10.1021/acs.chemmater.3c02114
Chem. Mater. 2024, 36, 730−741

performed using a Kratos Analytical Axis Supra spectrophotometer equipped with a dual-source Al/Ag monochromatic X-ray source and a charge neutralizer. The typical spot sizes for these measurements are approximately 500 μm in diameter. For the XPS measurements, samples of Sb_2Se_3@CNTs, CNTs, and bulk Sb_2Se_3 single crystals were mounted onto a dual height sample holder using carbon tape as adhesive. Fitting and analyses of the resulting XPS spectra were carried out by using the *CasaXPS* software.

2.7. Raman Spectroscopy. The Raman spectra of Sb_2Se_3@CNTs, empty CNTs, and bulk Sb_2Se_3 crystals were collected on a micro-Raman system based on Renishaw Inc. inVia microscope equipped with both a 785 nm and a 532 nm laser. Temperature-dependent cryogenic measurements (room temperature and at 93 K) were performed by mounting samples onto a Linkam THMS600 cryostat stage and built-in thermostat with a standard operational range of about 80−500 K. Typical Raman measurements were performed with a nominal power of 0.103 mW, 10 s exposure time, and 1−5 accumulations. The peak hardening of the G^+-bands was assessed by peak fitting in MagicPlot Pro with two Lorentzian peaks and a spline background. The peak maxima were extracted, and the differences between the empty CNT and Sb_2Se_3@CNT peak maxima were taken. The broadening of the G^--band, on the other hand, was assessed by extracting the full width at half-maximum (fwhm) of each peak. The Raman shifts observed at 532 nm excitation were validated by measuring samples that were dispersed onto 300 nm SiO_2/Si substrates (University Wafers). The Raman spectra of the samples and the underlying Si in the SiO_2/Si substrate in multiple random spots in these samples were taken. The Si peak from the SiO_2/Si substrate observed from each spectrum was used as an internal standard calibration peak and was fitted by using MagicPlot Pro with one Lorentzian peak and a spline background. The Raman spectra were calibrated by manually adjusting these fitted Si peaks to 520.7 cm^{-1}. Upon calibration, the G-bands were fit with two Lorentzian peaks each and the peak maxima were extracted and averaged. The difference in the Sb_2Se_3@CNT and the empty CNT G^+-band averages was taken.

2.8. Diffuse Reflectance Spectroscopy (DRS). Composite samples for DRS measurements were prepared by individually grinding Sb_2Se_3@CNTs, CNTs, and bulk Sb_2Se_3 crystals with spectroscopic grade potassium bromide (KBr, >99% trace metal basis, Sigma-Aldrich). These dilute samples were packed and compressed onto a custom-made holder with a transparent quartz window. DRS measurements on these as-prepared samples were performed on a Jasco V-670 spectrometer equipped with a 60-mm integrating sphere (Jasco ISN-923) which operates at a working range of 190−2500 nm. The resulting diffuse reflectance spectra were converted using the Kubelka−Munk function $(F(R_\infty))$[72] to approximate the absorbance profiles of the samples.

2.9. Liquid-Phase Ultraviolet−Visible (UV−Vis) Absorbance Spectroscopy. Individual dilute suspensions of Sb_2Se_3@CNTs and CNTs were prepared by sonicating the samples in *i*-PrOH (approximately 0.1 mg/mL loading) for 1 h. Immediately after sonication, room temperature absorption spectra of the resulting suspensions in the 200−800 nm range were collected using an Agilent Cary 100 UV−vis spectrophotometer. Pure *i*-PrOH was used as a blank solution.

2.10. First-Principles Density Functional Theory (DFT) Calculations of the Sb_2Se_3@CNT Heterostructure. DFT calculations were performed to determine the electron density difference map of a single chain of Sb_2Se_3 encapsulated within a (21,0) zigzag CNT. This (*n*,*m*) CNT index falls within the suitable range that corresponds to the 1.6 ± 0.4 nm diameter CNT used in our studies. All DFT calculations were conducted using the Cambridge Serial Total Energy Package, CASTEP academic 22.11 release.[73] Generalized gradient approximation with Perdew−Burke−Ernzerhof parametrization and Grimme's DFT-D2 vdW correction were used with on-the-fly generation ultrasoft pseudopotentials.[74,75] Real-space mesh cutoff of 400 eV was used for all DFT calculations. For the Sb_2Se_3@CNT system, a periodic boundary condition supercell of a single chain of Sb_2Se_3 in a (21,0) CNT was built where the long axis ([010] direction) of the Sb_2Se_3 chain was aligned to the *z*-axis of the CNT. The supercells that were constructed for the Sb_2Se_3@CNT heterostructure considered one- and two-unit cell lengths along the crystallographic [010] direction of the Sb_2Se_3 crystal structure. The supercell system was then energy minimized using a Monkhorst−Pack *k*-point mesh at Gamma until the total energies converge to 10^{-5} eV per atom and displacements less than 0.001 Å. The electron density difference map was calculated using the optimized geometry with a Monkhorst−Pack *k*-point mesh of 1 × 1 × 15. Bader atomic charges of the systems were calculated using electron density from the final single-point CASTEP calculation with the help of den2VASP and Bader charge analysis codes.[76,77]

3. RESULTS AND DISCUSSION

The distinction between the bulk single crystal habit and the micromechanically cleaved microstructure of Sb_2Se_3 presented a platform to investigate the propensity of the q-1D vdW $[Sb_4Se_6]_n$ chains to form quasi-2D sheets when exfoliated from top-down routes. As previously discussed, this stark difference points toward the anisotropic interchain vdW interactions that arise from the significant interplay between the stereochemically active Sb 5s lone pairs and the Se 4p orbitals along the [001] direction. To validate the experimental manifestation of vdW anisotropy and its influence on the nanoscale morphology of Sb_2Se_3, we exfoliated single crystals of Sb_2Se_3 using top-down liquid phase exfoliation techniques and characterized the resulting nanostructures using HRTEM (Figure 2). Based on the bulk Sb_2Se_3 crystal structure alone (Figure 2A), the one-dimensional nature of the ordered $[Sb_4Se_6]_n$ chains suggests a combination of nanowire bundles, nanoribbons, or quasi-2D

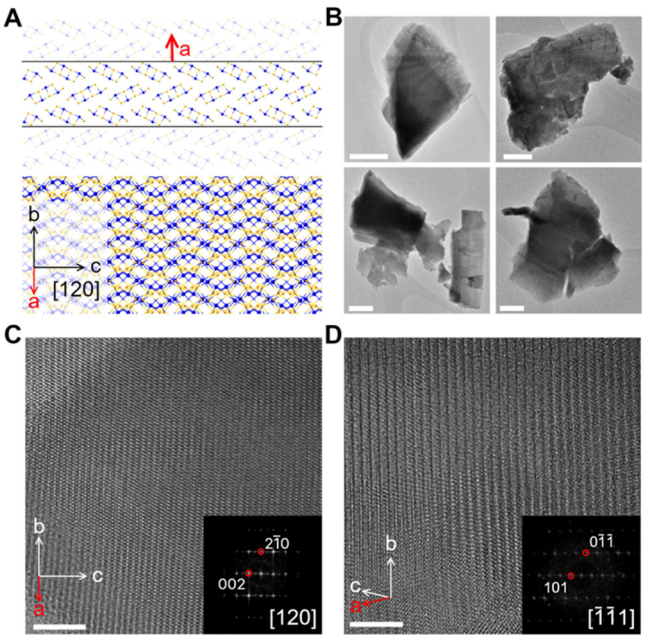

Figure 2. Quasi-2D Sb_2Se_3 nanoribbons and nanosheets derived from top-down liquid-phase exfoliation. (A) Representative crystal structure of Sb_2Se_3 highlighting the *a*-axis ([100] direction, top) as the likely orientation of the exfoliated sheets. Shown in the bottom panel is one of the observed zone axes in the [120] direction, which shows an *a*-axis character (*h*00) and a slight *c*-axis (00*l*) tilt. (B) Low-magnification TEM images of the quasi-2D Sb_2Se_3 nanosheets and nanoribbons. Scale bars: 200 nm. (C, D) High-magnification HRTEM images of the quasi-2D nanostructures. Inset: corresponding FFTs and zone axis orientations indexed from the bulk crystal structure. Scale bars: 5 nm.

https://doi.org/10.1021/acs.chemmater.3c02114
Chem. Mater. 2024, 36, 730−741

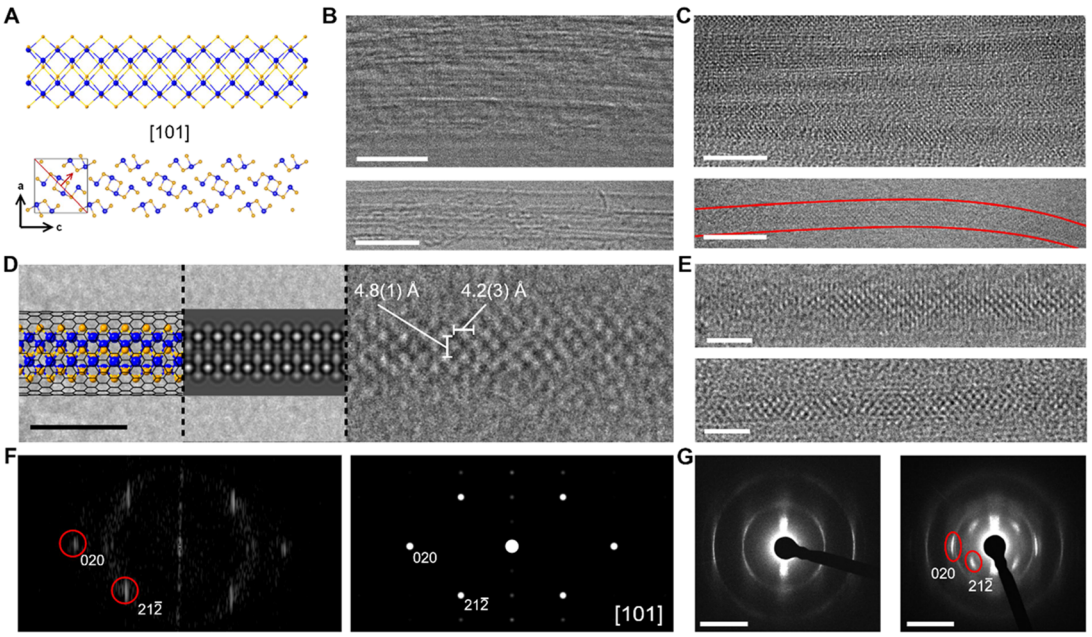

Figure 3. HRTEM and SAED analysis of isolated single chains of $[Sb_4Se_6]_n$in the Sb_2Se_3@CNT heterostructure. (A) Crystal structure model of a single covalent chain of $[Sb_4Se_6]_n$ oriented along the [101] zone axis of the Sb_2Se_3 crystal. The *b*-axis was oriented horizontal to the page (top) and out-of-the page (bottom). (B) Partially defocused HRTEM of empty CNT bundles (top) and a few isolated nanotubes (bottom). Scale bar: 5 nm. (C) HRTEM of a bundle (top) and an isolated (bottom) Sb_2Se_3@CNT heterostructure. Red lines added as a guide to the eye highlight the uniformity of the crystalline structure along the length of the CNT. Scale bar: 5 nm. (D) Model Sb_2Se_3@CNT representation with the $[Sb_4Se_6]_n$ chain oriented along the [101] zone (left), simulated HRTEM of a single covalent chain of Sb_2Se_3 along the [101] zone (center), and experimental HRTEM image of an isolated Sb_2Se_3@CNT heterostructure. Average extrapolated atomic distances of the Sb(1)−Sb(1) and Sb(1)−Sb(2) sites are indicated. Scale bar: 2 nm. (E) Additional representative images of isolated Sb_2Se_3@CNT wires. Scale bar: 2 nm. (F) FFT of the experimental HRTEM image of the Sb_2Se_3@CNT heterostructure in D (left) and simulated diffraction pattern of a [101]-oriented Sb_2Se_3 (right). (G, left) SAED of a bundle of empty CNTs with only diffuse diffraction rings from randomly oriented CNTs visible. (G, right) SAED of the bundle of Sb_2Se_3@CNT from (C) showing crystalline diffraction spots consistent with a preferred orientation along the [101] zone axis (right). Scale bars: 5 nm^{-1}.

nanosheets upon top-down exfoliation along the various vdW axes in the basal plane direction. However, when imaged under HRTEM, we observed only nanostructures that have quasi-2D morphologies such as nanoribbons and nanosheets with little to no signs of any 1D-like nanostructure (Figure 2B). The resulting sheet-like structures behaved like exfoliated nanosheets from 2D vdW crystals, which are often found to preferentially stack on top of each other and show thin layered-like step edges.[39]

Upon closer inspection of these well-defined and highly crystalline sheet-like nanostructures, we found from indexing the FFTs of representative HRTEM micrographs that the as-deposited and nontilted quasi-2D nanostructures were oriented along the [120] or [111] zone axes (Figure 2A,C,D). These observed orientations suggest that Sb_2Se_3 sheets cleave primarily along the [100] direction, which corresponds to the direction that has the longest interatomic distances and consequently weakest vdW interactions. Cleavage along this direction thereby preserves the crystalline order along the *b*-axis ([010] direction), which corresponds to the covalent long axis, and the *c*-axis ([001] direction), which corresponds to the crystallographic orientation of the stronger interchain interactions from the stereochemically active lone pairs. These results are consistent with the analyses of the different bonding interactions in Sb_2Se_3 and further support the strong role of the stereochemically active lone pair interactions in driving the morphology of exfoliated Sb_2Se_3 nanostructures. The manifestation of the stronger interactions, as we have shown herein, significantly limits the capability of top-down exfoliation routes to access single chains from Sb_2Se_3.

To overcome the significant interchain bonding interactions in Sb_2Se_3, we utilized single-walled CNTs to encapsulate the single chains of $[Sb_4Se_6]_n$ (Figure 3). We were able to readily access the encapsulation of Sb_2Se_3 within CNTs via capillary action in a mixed-melt growth[61,63,64] in which a large excess of crystalline Sb_2Se_3 powders (Figure S1) were combined with CNTs that were air-annealed to open the ends. For our studies, we used Sb_2Se_3 as a model phase for pnictogen chalcogenides due to the lower vapor pressure of Se (compared to Sb_2S_3), its existence as the only line compound in the Sb−Se binary phase diagram, and its accessible melting temperature of about 600 °C.[78] Due to the expected density mismatch between the CNT surface of the Sb_2Se_3@CNT heterostructure and the Sb_2Se_3 melt, the resulting solids readily phase separated from the solidified melt making Sb_2Se_3@CNT easily isolable (Figure S2). Furthermore, this facile separation of the heterostructure product from the melt could have also arisen from the pristine nature of the CNT source that we used for the syntheses, which are unlikely to introduce nucleation sites for residual Sb_2Se_3 from the melt to adhere to the surface. We extracted the Sb_2Se_3@CNT heterostructures from the bulk solidified melt of Sb_2Se_3 with no further purification necessary. The structure, phase purity, and extent of filling of the resulting Sb_2Se_3@CNT heterostructure were established by comparing the HRTEM images of empty and filled CNTs (Figures 3A−E and S3, S4). From these micrographs, a clear contrast difference can be observed between the empty and filled tubes, with empty tubes

https://doi.org/10.1021/acs.chemmater.3c02114
Chem. Mater. 2024, 36, 730−741

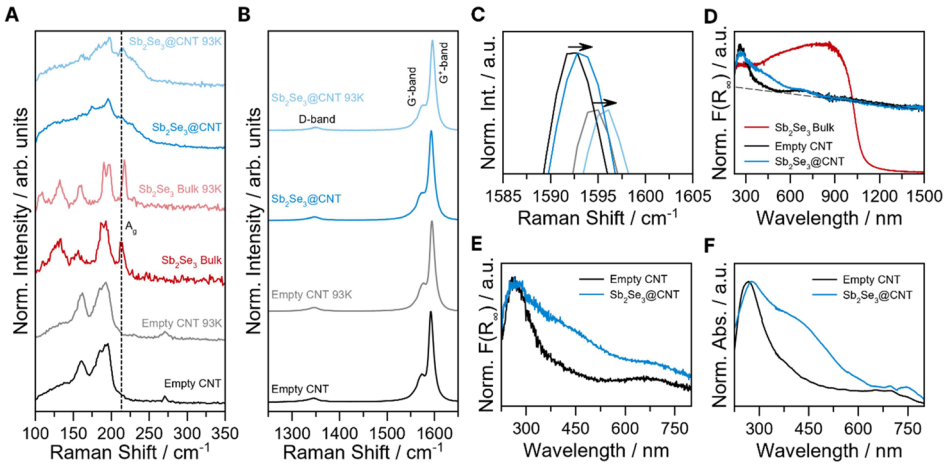

Figure 4. Ensemble Raman and absorption spectroscopy of Sb_2Se_3@CNT. (A) Temperature-dependent Raman spectroscopy of empty CNTs, a bulk Sb_2Se_3 crystal, and Sb_2Se_3@CNT heterostructure ensemble in the CNT RBM spectral region at room temperature and at 93 K. The low-temperature, 93 K, spectra were plotted using a lighter and more translucent shade to distinguish it from the room temperature spectra. (B) Temperature-dependent Raman spectra of the Sb_2Se_3@CNT heterostructure and empty CNTs in the spectral region that shows the single-walled CNT D- and (G^-/G^+)-bands at room temperature and at 93 K. (C) Magnified representation of CNT G^+-band hardening upon filling of $[Sb_4Se_6]_n$. For clarity, the intensity of the 93 K G^+ bands represented as lighter translucent curves were arbitrarily shifted down by a nominal value. (D) Kubelka–Munk absorbance plots of bulk Sb_2Se_3 powders, Sb_2Se_3@CNT heterostructure, and empty CNTs obtained from diffuse reflectance spectroscopy. (E) Magnified representation of the Kubelka–Munk absorbance region highlighting the emergent absorption features in the Sb_2Se_3@CNT heterostructure compared to the empty CNTs. (F) UV–vis absorption spectra of *i*-PrOH suspensions of empty CNTs and Sb_2Se_3@CNT.

even needing to be partially defocused to be visible (Figure 3B,C). Interestingly, by accounting for the continuous higher contrast arising from the filling of Sb_2Se_3 within the nanotubes both in HRTEM and STEM imaging, the encapsulation methodology that we employed had a filling efficiency close to ~100%, with little to no empty CNTs found throughout the representative TEM grid (Figures S3 and S5). We attribute this filling efficiency to the pristine quality and long-range uniformity of the single-walled CNTs that we used in this study (see the 2).

Close inspection of the high-magnification micrographs of the Sb_2Se_3@CNTs also show highly uniform periodicity as evidenced by the consistent lattice fringes that can be indexed closest to [101]-oriented single chains from the parent Sb_2Se_3 bulk crystal structure (Figures 3A,D,E and S6). The matching of these high-resolution HRTEM images to the crystal structure model and simulated HRTEM pattern[71] of a single chain derived from the experimental single crystal structure of Sb_2Se_3[40] indicates that there is minimal structural modulation in the chain upon encapsulation within a CNT. Specifically, we found that there were minimal bond distance differences between the direct comparison of the atomic distances of the Sb(1)–Sb(1) crystallographic sites (or Sb(2)–Sb(2); along the chain direction) and Sb(1)–Sb(2) sites (perpendicular to the chain direction) derived from the single crystal structure as compared to the experimental distances measured from HRTEM imaging of Sb_2Se_3@CNT. These atomic distance differences in the Sb(1 or 2)–Sb(1 or 2) sites (3.99 Å in the bulk versus 4.2(3) Å in the single chain) and Sb(1)–Sb(2) sites (4.77 Å in the bulk versus 4.8(1) Å in the single chain) are well within the error of the HRTEM measurement and the standard deviation from multiple sites. From a bond distance and symmetry perspective, these results are suggestive of the preservation of the general bulklike structure of the $[Sb_4Se_6]_n$ chains upon encapsulation. We also found from HRTEM studies of ambient exposed Sb_2Se_3@CNT heterostructures (Figure S5) that the lattice fringes are persistent after a 2-month exposure period which shows that encapsulation does not only enable the isolation of single chains but also protect these chains from degradation or surface oxidation. Furthermore, elemental analyses of Sb_2Se_3@CNT ensembles and single chains from SEM-energy dispersive X-ray spectroscopy (SEM-EDS) and STEM-EDS analyses indicate that there is a ~2:3 elemental ratio of Sb and Se which is in good agreement with the bulk crystal stoichiometry and composition (Figure S4). Additionally, ensemble XPS was used to confirm the purity of Sb_2Se_3 and to ensure that there were no competing structures with varied chemical environments were present in the sample (Figures S7 and S8; Table S1). From these experiments, the observed Sb 3d and Se 3d peaks in the spectra both match the binding energies of the equivalent peaks of the bulk structure well within ~0.1 eV difference.[37,79] Although the Sb $3d_{5/2}$ peak overlaps with the O 1s peak, which is likely adventitious or oxidized CNT in origin, the lack of any additional higher binding energy shoulders or significant peak broadening indicates that no oxides of Sb are present in the heterostructure. These results suggest that, within the resolution of our instrumentation, there is only minimal perturbation of the chemical environment of the $[Sb_4Se_6]_n$ chains when encapsulated within the CNT. Altogether the close resemblance of the crystal structure and elemental composition of the as-grown Sb_2Se_3@CNT heterostructure indicates that encapsulation within CNTs is a viable route to isolate chains derived from highly anisotropic q-1D vdW crystals with minimal structural or chemical perturbation from the bulk structure.

Further analyses of the structure of Sb_2Se_3@CNT revealed insights as to how the guest $[Sb_4Se_6]_n$ chain influences the assembly of the heterostructure bundles. Strikingly, the FFT of the high-magnification HRTEM image of a single Sb_2Se_3@CNT heterostructure (Figure 3F) and the SAED of a Sb_2Se_3@CNT bundle (Figure 3G, right) compared to an empty CNT bundle (Figure 3G, left) showed that $[Sb_4Se_6]_n$ chains are mainly oriented close to the [101] crystallographic zone axis of

https://doi.org/10.1021/acs.chemmater.3c02114
Chem. Mater. 2024, 36, 730–741

Sb_2Se_3, indicative of a preferred orientation of the chains along this edge. As expected, the lack of any *b*-axis contribution in the indexed zone axis confirms that the covalent axis is confined to the same direction as the long axis of the CNT. The preferential orientation along the [101] zone, nevertheless, is surprising. In the context of an isolated single chain of Sb_2Se_3 outside of a CNT, a single chain with a rectangular cross-section will lay flat along the longer edge of the cross-section. Based on the bulk crystal structure of Sb_2Se_3, this orientation corresponds closest to the observed [101] zone axis (Figure 3A). Within the CNT, the preferential orientation along the [101] zone became more intriguing. We infer that a guest-induced anisotropic swelling along the basal plane of the CNT arises from the rectangular cross-section of the $[Sb_4Se_6]_n$ chain and hinders the rotational freedom of Sb_2Se_3@CNT as an isolated heterostructure or in an ensemble. The rectangular cross-section of the guest $[Sb_4Se_6]_n$ chain could distort the cross-section of the CNT, forcing one cross-sectional direction to distort further from the terminal Se atoms and another (perpendicular) cross-sectional direction to distort closer to the long cross-sectional edge of the $[Sb_4Se_6]_n$ chain. In this scenario, the circular cross-section of the CNT will take on an ellipsoid shape, which subsequently causes the Sb_2Se_3@CNT heterostructures to lay along the long edge of the ellipsoid as it deposits on the TEM grid. This anisotropic cross-sectional behavior in CNTs has been similarly observed in the encapsulation of helical CsI within CNTs, where the encapsulation caused the anisotropic bending of the CNT as the CsI chain twisted.[58] Other possible high-symmetry crystallographic orientations of single chains were not observed in the Sb_2Se_3@CNT heterostructures (Figure S9). Experimental support for this conjecture was also found in the form of the broadening of the graphitic G^- Raman mode in CNT upon encapsulation of the $[Sb_4Se_6]_n$ chain (Figure S10). The G^- mode corresponds to the vibration of the lateral C−C bonds in the CNT and is expected to broaden due to the stretching and shortening of the C−C bonds as the CNT assumes an asymmetric ellipsoid-like cross-section in the Sb_2Se_3@CNT heterostructure. We note that further evidence to support this observation is beyond the scope of the current study.

Complementary to the structural analyses via electron microscopy, the ensemble Raman response of the Sb_2Se_3@CNT heterostructures was investigated using 532 nm (Figures 4A−C and S10) and 785 nm (Figures S10 and S11) excitation wavelengths. In these experiments, we observed that the majority of the Sb_2Se_3 Raman signals are obscured and convoluted by the intense radial breathing modes (RBMs) of the CNTs.[80] However, in the spectral region above 200 cm^{-1}, further comparison of the empty CNT and Sb_2Se_3@CNT Raman spectra excited at 532 nm revealed a distinct peak in the spectrum of the Sb_2Se_3@CNT that closely matches the Sb_2Se_3 Raman-active peaks corresponding to the closely spaced B_{1g} and A_g modes at 212 to 213 cm^{-1} (Figure 4A).[81,82] The peaks become more noticeable at the low-temperature, 93 K, spectra, where the Raman peaks are generally narrower and confirm the persistence of the Sb_2S_3 chain structure upon encapsulation. Beyond these closely spaced peaks, attempts to disambiguate other Sb_2Se_3 Raman-active modes using the room temperature and 93 K spectra at both 532 nm (Figure 4A) and 785 nm (Figure S11) excitations proved to be difficult due to the prominent series of CNT RBMs that are concentrated below 200 cm^{-1}. The observed broadening and slight shifting of the Raman peak arising from the Sb_2Se_3 B_{1g} and A_g vibrational modes as compared to the bulk is consistent with the substantial confinement of the $[Sb_4Se_6]_n$ chains from the bulk down to single isolated chains. General trends of Raman modes shifting to higher frequencies at lower temperatures were consistent with the expected temperature-induced lattice contraction of the structures involved (empty CNTs, Sb_2Se_3 bulk, and Sb_2Se_3@CNT).

Beyond the low-energy Raman spectral window, we also looked into the region which covers the signature phonon modes of single-walled CNTs (Figures 4B,C and S10, S11). Specifically, we probed the longitudinal (G^+-band) and lateral (G^--band) graphitic phonon modes and the defect-induced lattice vibrations (D-band) within the Raman spectral region between 1200 and 1700 cm^{-1}.[80] We observed no significant peak shift or peak broadening in the D-bands upon encapsulation of Sb_2Se_3 in the CNT (Figure 4B). Additionally, the intensity of the D-band relative to the G-bands in the Raman spectra of the Sb_2Se_3@CNT heterostructure remained unchanged as compared to the empty CNTs, indicating that the filling of CNTs with Sb_2Se_3 did not introduce additional defects to the highly ordered lattice of the host CNT. The longitudinal G^+-band, on the other hand, showed expected hardening upon filling across the two excitation wavelengths (532 and 785 nm) and temperatures (room temperature and 93 K) that we used. These shifts corresponding to the peak maxima differences of the G^+-band of the filled and empty CNTs correspond to the following fitted values: +0.62 cm^{-1} at 532 nm (RT), +0.92 cm^{-1} at 532 nm (93K), +1.20 cm^{-1} at 785 nm (RT), and +1.42 cm^{-1} at 785 nm (93K) (Figure S10). While this behavior is consistent with other CNT encapsulation studies, the shifts that we determined were found to fall close to the instrumental limitations of our Raman spectrometer (~1 cm^{-1} resolution) and were small relative to other literature reports (Figures 4C and S10).[57,62] To systematically validate the shifts that we observed, multiple spots of a thinly dispersed sample on a 300 nm SiO_2/Si substrate were sampled. These thin films of Sb_2Se_3@CNT enabled the observation of Raman-active modes of the underlying substrate alongside the Sb_2Se_3@CNT peaks. The first-order Raman peak of Si from the substrate was used as an internal standard and was calibrated to 520.7 cm^{-1}. Upon calibration, only nominal shifts of the Si peak on the order of ±0.01 to 0.3 cm^{-1} were necessary, confirming the consistent hardening of the G^+ mode that we observed prior. The G^+-band extrapolated from the calibrated room temperature 532 nm spectra yielded an average fitted value of 0.81 ± 0.38 cm^{-1} revealing that there is, indeed, a hardening of the G^+-band in the Sb_2Se_3@CNT heterostructure (further details described in the 2). No appreciable shifts of the lateral G^--bands were found between the empty and the filled CNTs. As discussed previously in the structural determination of Sb_2Se_3@CNT, a broadening in the lateral band was observed, with the fwhm at room temperature and 532 nm excitation wavelength increasing from 19.6 ± 0.4 cm^{-1} in empty CNTs to 21.7 ± 0.6 cm^{-1} in the Sb_2Se_3@CNT spectra. The broadening observed could indicate anisotropic lateral stretching of the CNT.

The successful creation of the Sb_2Se_3@CNT heterostructure enabled us to gain further insights on the evolution of the optical properties of the Sb_2Se_3 crystal upon encapsulation as a single chain within a CNT. The ensemble absorbance properties of the Sb_2Se_3@CNT heterostructure were examined

https://doi.org/10.1021/acs.chemmater.3c02114
Chem. Mater. 2024, 36, 730−741

by room temperature DRS of the samples dispersed in a KBr matrix and UV−vis spectroscopy of samples suspended in *i*-PrOH (Figure 4D−F). Direct comparison of the Kubelka−Munk (K−M) absorbance ($F(R_\infty)$) profiles derived from the DRS measurements of the empty CNTs, bulk Sb_2Se_3 microcrystallites, and Sb_2Se_3@CNTs revealed several distinguishing features which demonstrate the influence of encapsulation on the optical properties of Sb_2Se_3 (Figure 4D). As expected, the K−M absorbance spectrum of the empty CNTs exhibited a broadband absorption profile with a maximum absorbance at approximately 266 nm, which is attributed to a $\pi \rightarrow \pi^*$ transition. A minimal shoulder trailing into higher wavelengths likely contributed by $n \rightarrow \pi^*$ transitions from carbonyl C═O groups from partial oxidation of the nanotube was also observed.[83] The K−M absorbance of the bulk Sb_2Se_3 microcrystallites, on the other hand, featured the expected characteristic band edge absorption at 1082 nm (1.15 eV).[37,44,48] Intriguingly, an absorbance edge at 1082 nm (1.15 eV) was absent in the Sb_2Se_3@CNT heterostructure. Instead, we noticed persistence of the CNT $\pi \rightarrow \pi^*$ transition and the emergence of a new edge-like absorbance feature with an onset at ∼600 nm in the Sb_2Se_3@CNT spectra (Figure 4E). To complement these measurements and better visualize this emergent absorption feature, we dispersed the empty CNTs and Sb_2Se_3@CNT samples in *i*-PrOH and collected the UV−vis absorption spectra of the suspensions. In contrast to the empty CNTs that appeared jet black in color, the Sb_2Se_3@CNT suspension displayed a maroon-like coloration from visual inspection, further supporting the observation of the emergent absorption feature in the visible range. UV−vis spectroscopy of the empty CNTs and Sb_2Se_3@CNT suspensions mirrored the K-M absorbance spectra but presented a better resolution of the CNT absorption maxima and absorption onset at around 600 nm (Figure 4F). With improved signal-to-noise ratios, we found that the Sb_2Se_3@CNT spectra exhibited a pronounced absorption discontinuity, indicating a blue-shifted band-like absorption edge compared to the bulk. Collectively, these spectroscopy results are consistent with quantum confinement-induced shifting of the Sb_2Se_3 band gap (blue-shifted by about 1 eV) upon encapsulation. Similar size-dependent behaviors have been predicted and observed in several nanostructures based on pnictogen chalcogenides.[42,43,84−87]

We performed first-principles DFT calculations[74,75,88] to complement our experimental observations and gain a better understanding of the possible electronic interactions that could arise from the encapsulation of a single $[Sb_4Se_6]_n$ chain inside CNT (Figure 5). In these calculations inspired by similar studies,[54,67] we considered the incommensurate lattice heterostructure formed by an achiral, narrow band gap host (21,0) CNT[89] which we chose due to the closeness of its diameter (∼1.57 nm) to the average diameter of the Tuball CNTs that we used (1.6 ± 0.4 nm) and the guest Sb_2Se_3, whose lattice parameters differ by about 6% along the covalent long-axis direction. Note that this Sb_2Se_3-to-CNT combination is a representative structure meant to illustrate one of the possible 136 unique (n,m) index combinations calculated strictly from the diameters of the CNTs comprising the Tuball ensemble used in this study.[90,91] From our initial attempts, we found that using a heterostructure that is one periodic unit cell long resulted in a stretching of the Sb_2Se_3 chain ∼7.5% larger than the bulk counterpart upon relaxation (Figure S12). Increasing the size of the model heterostructure to a supercell

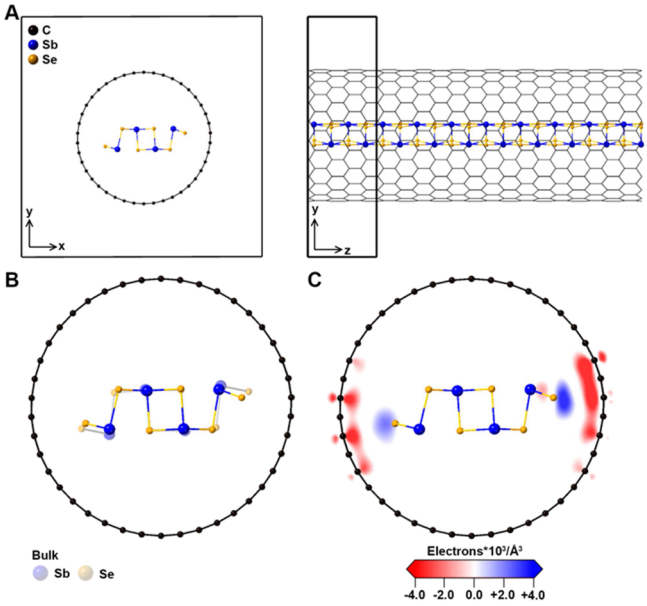

Figure 5. Energy-minimized atomic structure and electron density calculations of the Sb_2Se_3@CNT heterostructure. (A) Energy-minimized atomic structure of the heterostructure formed by a $[Sb_4Se_6]_n$ chain encapsulated within a (21,0) zigzag CNT. These were calculated with two periodic units in the heterostructure supercell and are projected along the basal plane (left) and the long-chain axis (right). The supercell dimensions equivalent to two-unit cell lengths along the [010] chain direction of Sb_2Se_3 are outlined in the right panel. For clarity, the CNT is represented as a skeletal framework in the projection along the *z*-direction of the CNT. (B) Comparison of the energy-minimized $[Sb_4Se_6]_n$ chain structure (opaque) with a single chain extracted from the experimental bulk crystal structure (translucent). (C) Spatial visualization of the electron density difference map resulting from the interaction of the host CNT and the guest $[Sb_4Se_6]_n$ chain. Due to the reconfiguration of the chain axis, we note that the *z*-axis of the CNT in this projection corresponds to the crystallographic *b*-axis ([010] direction) of the Sb_2Se_3 structure.

with two periodic unit cell lengths of Sb_2Se_3 decreased the strain to 6.4% along the covalent axis but showed a dramatic increase in computation time due to the 188-atom supercell. Any larger supercell that we attempted was too computationally expensive for our purposes, offering diminishing returns in relaxing the incommensurate lattice. Because of this computational limitation, we refrained from extrapolating the electronic band structure of Sb_2Se_3@CNT and focused on the qualitative aspects that we can derive from our calculations. As such, we were able to calculate a minimal anisotropic electron donation from the host CNT into the terminal divalent Se atoms of the guest $[Sb_4Se_6]_n$ chain. The qualitative electron transfer behavior we observed from the CNT to the $[Sb_4Se_6]_n$ chain is consistent with other chalcogenide-terminated species encapsulated within CNTs.[53,67] Spatial visualization of the electron density difference map reveals that the anisotropic interaction between the guest and host is reminiscent of the bulk crystal structure in which there is a weak, but significant, attraction of neighboring atoms in adjacent $[Sb_4Se_6]_n$ chains onto the highly electronegative terminal Se atoms. Inspired by these observations, we performed Bader charge analysis to further assess the degree of guest−host interactions in this specific Sb_2Se_3−CNT combination that we used. From these analyses, we found that only 0.163 electrons were donated by the CNT to the $[Sb_4Se_6]_n$ chain across two unit cells (0.0815*e*

https://doi.org/10.1021/acs.chemmater.3c02114
Chem. Mater. 2024, 36, 730−741

per unit cell). This value is commensurate with other encapsulated vdW systems and is significantly smaller than encapsulated systems based on structures with broken covalent bonds.[52,67,92−95] Moreover, this minimal electron reorganization, in addition to very little structural perturbation in the experimental structure, points to the blue shift in the absorbance onset, likely resulting from the confined Sb_2Se_3 guest chain rather than a donor−acceptor interaction. Finally, the simulated structures also revealed that while there was minimal deformation of the Sb−Se bond lengths (<0.05 Å; 0.04 to 1% difference), the significant modulation of the Sb−Se−Sb and Se−Sb−Se bond angles (8−10% difference) that occurred after energy minimization accounted for the 6.4% lattice expansion that was apparent in the energy-minimized structures (Figure S13). The minimal calculated differences in the bond distances are consistent with the measurable bond distances obtained from the $[Sb_4Se_6]_n$ chain structure that we experimentally observed within the Sb_2Se_3@CNT heterostructure. Our comparison of the bond angles to experimental measurements, on the other hand, is limited by the orientation and resolution of our microscopy data. Furthermore, we reiterate that these computational results (and the associated mismatch) are specific to only the combination of Sb_2Se_3 and (21,0) CNT.

4. CONCLUSIONS

In this article, we demonstrated that CNT encapsulation is a facile approach to access single chain analogues of 1D and q-1D vdW crystals that exhibit strong and anisotropic interchain interactions. We established through a series of structural and spectroscopic probes that an encapsulated single chain of Sb_2Se_3 maintains its structural integrity and displays little to no significant distortion of the chain structure compared to the bulk crystal structure. When a suitable diameter-matched host nanotube is available, these findings suggest that the encapsulation of 1D and q-1D vdW phases in well-defined CNTs is an ideal system to study single chain properties with minimal structural perturbation. We also systematically demonstrated the influence of extreme vdW confinement on the intrinsic phonon modes and electronic states in Sb_2Se_3, highlighting the emergence of a band-like absorption collectively indicative of a significant blue shift of the Sb_2Se_3 band gap from the NIR well into the visible range and emergent host−guest interactions. The enhanced visible range absorption of the Sb_2Se_3@CNT heterostructures, coupled with the projected improvement of electron transport along 1D chains, poises these materials as building blocks in high-speed optoelectronic devices in spectral windows relevant to next-generation sensing and energy-harnessing technologies. Our results, together with previous demonstrations of confined growth within CNTs, could be further expanded to the growing number of atomically precise vdW nanotubes with various compositions, including hexagonal boron nitrides and transition metal dichalcogenide nanotubes.

■ ASSOCIATED CONTENT

Data Availability Statement

All data are available in the main text or the Supporting Information.

Supporting Information

The Supporting Information is available free of charge at https://pubs.acs.org/doi/10.1021/acs.chemmater.3c02114.

Supplementary data and results: experimental and calculated PXRD of bulk precursor crystals; representative optical image of the resulting mixed melt growth products that produce Sb_2Se_3@CNT; additional TEM and STEM images of the Sb_2Se_3@CNT samples; EDS of the Sb_2Se_3@CNT samples taken by both SEM and STEM; ambient air exposure HRTEM study of Sb_2Se_3@CNT samples; HRTEM image of an isolated Sb_2Se_3@CNT depicted in Figure 3D; XPS survey spectra of the empty CNTs, Sb_2Se_3 bulk, and Sb_2Se_3@CNT samples; fitted high-resolution XPS peaks from empty CNTs, Sb_2Se_3 bulk, and Sb_2Se_3@CNT samples; crystal structure models depicting possible high-symmetry orientations of a single Sb_2Se_3 chain; additional temperature-dependent Raman analysis of the G-band region of the spectra obtained from empty CNTs and Sb_2Se_3@CNT samples with peak fits for both 532 and 785 nm excitation wavelengths; additional temperature-dependent Raman spectra of empty CNTs, Sb_2Se_3 bulk, and Sb_2Se_3@CNT samples taken using 785 nm excitation wavelength; calculated atomic structure and electron density difference of a one-unit-cell-long Sb_2Se_3 chain encapsulated in a (21,0) nanotube; calculated atomic structure of a relaxed two-unit-cell-long Sb_2Se_3 chain within a CNT and in the bulk crystal structure; and summary of the high-resolution XPS peak fitting parameters derived from the fitted peaks in Figure S8 (PDF)

■ AUTHOR INFORMATION

Corresponding Author

Maxx Q. Arguilla − *Department of Chemistry, University of California Irvine, Irvine, California 92697, United States;* orcid.org/0000-0001-9948-0814; Email: marguill@uci.edu

Authors

Griffin M. Milligan − *Department of Chemistry, University of California Irvine, Irvine, California 92697, United States;* orcid.org/0000-0002-6632-8004

Ze-Fan Yao − *Department of Chemistry and Department of Chemical and Biomolecular Engineering, University of California Irvine, Irvine, California 92697, United States;* orcid.org/0000-0001-5590-0768

Dmitri Leo Mesoza Cordova − *Department of Chemistry, University of California Irvine, Irvine, California 92697, United States*

Baixin Tong − *Department of Chemistry, University of California Irvine, Irvine, California 92697, United States*

Complete contact information is available at: https://pubs.acs.org/10.1021/acs.chemmater.3c02114

Author Contributions

G.M.M.: methodology, investigation, visualization, and writing—original draft preparation; Z.Y.: methodology, investigation, and writing—reviewing and editing; D.L.M.C.: methodology, investigation, and writing—reviewing and editing; B.T.: investigation; M.Q.A.: conceptualization, supervision, and writing—reviewing and editing.

Notes

The authors declare no competing financial interest.

https://doi.org/10.1021/acs.chemmater.3c02114
Chem. Mater. 2024, 36, 730−741

■ ACKNOWLEDGMENTS

The authors would like to acknowledge the UC Irvine Department of Chemistry Laser Spectroscopy Laboratories for instrumental support. G.M.M. and M.Q.A. thank Dr. Toshihiro Aoki for valuable support during preliminary electron microscopy experiments, Dr. Ich Tran for his extensive assistance during XPS measurements, and Mr. Franco Miranda Romero for his programming expertise and assistance in data analysis. Several aspects of this work were performed at the UC Irvine Materials Research Institute (IMRI). Facilities and instrumentation at IMRI are supported, in part, by the National Science Foundation through the UC Irvine Materials Research Science and Engineering Center grant number DMR-2011967. XPS was performed using instrumentation funded in part by the National Science Foundation Major Research Instrumentation Program under grant number CHE-1338173.

■ REFERENCES

(1) Blumenstein, C.; Schäfer, J.; Mietke, S.; Meyer, S.; Dollinger, A.; Lochner, M.; Cui, X. Y.; Patthey, L.; Matzdorf, R.; Claessen, R. Atomically controlled quantum chains hosting a Tomonaga−Luttinger liquid. *Nat. Phys.* **2011**, *7* (10), 776−780.

(2) Shumiya, N.; Hossain, M. S.; Yin, J. X.; Wang, Z. W.; Litskevich, M.; Yoon, C.; Li, Y. K.; Yang, Y.; Jiang, Y. X.; Cheng, G. M.; et al. Evidence of a room-temperature quantum spin Hall edge state in a higher-order topological insulator. *Nat. Mater.* **2022**, *21* (10), 1111−1115.

(3) Schindler, F.; Wang, Z.; Vergniory, M. G.; Cook, A. M.; Murani, A.; Sengupta, S.; Kasumov, A. Y.; Deblock, R.; Jeon, S.; Drozdov, I. Higher-order topology in bismuth. *Nat. Phys.* **2018**, *14* (9), 918−924.

(4) Schmaus, S.; Bagrets, A.; Nahas, Y.; Yamada, T. K.; Bork, A.; Bowen, M.; Beaurepaire, E.; Evers, F.; Wulfhekel, W. Giant magnetoresistance through a single molecule. *Nat. Nanotechnol.* **2011**, *6* (3), 185−189.

(5) Geim, A. K.; Novoselov, K. S. The rise of graphene. *Nat. Mater.* **2007**, *6* (3), 183−191.

(6) Bhimanapati, G. R.; Lin, Z.; Meunier, V.; Jung, Y.; Cha, J.; Das, S.; Xiao, D.; Son, Y.; Strano, M. S.; Cooper, V. R.; et al. Recent Advances in Two-Dimensional Materials beyond Graphene. *ACS Nano* **2015**, *9* (12), 11509−11539.

(7) Mannix, A. J.; Kiraly, B.; Hersam, M. C.; Guisinger, N. P. Synthesis and chemistry of elemental 2D materials. *Nat. Rev. Chem.* **2017**, *1* (2), No. 0014.

(8) Schaibley, J. R.; Yu, H. Y.; Clark, G.; Rivera, P.; Ross, J. S.; Seyler, K. L.; Yao, W.; Xu, X. D. Valleytronics in 2D materials. *Nat. Rev. Mater.* **2016**, *1* (11), 16055.

(9) Tang, L.; Tan, J.; Nong, H.; Liu, B.; Cheng, H.-M. Chemical vapor deposition growth of two-dimensional compound materials: controllability, material quality, and growth mechanism. *Acc. Mater. Res.* **2021**, *2* (1), 36−47.

(10) Novoselov, K. S.; Jiang, Z.; Zhang, Y.; Morozov, S. V.; Stormer, H. L.; Zeitler, U.; Maan, J. C.; Boebinger, G. S.; Kim, P.; Geim, A. K. Room-temperature quantum hall effect in graphene. *Science* **2007**, *315* (5817), 1379−1379.

(11) Tran, K.; Moody, G.; Wu, F. C.; Lu, X. B.; Choi, J.; Kim, K.; Rai, A.; Sanchez, D. A.; Quan, J. M.; Singh, A.; et al. Evidence for moire excitons in van der Waals heterostructures. *Nature* **2019**, *567* (7746), 71−75.

(12) Zhang, Y. B.; Tan, Y. W.; Stormer, H. L.; Kim, P. Experimental observation of the quantum Hall effect and Berry's phase in graphene. *Nature* **2005**, *438* (7065), 201−204.

(13) So, J. P.; Kim, H. R.; Baek, H.; Jeong, K. Y.; Lee, H. C.; Huh, W.; Kim, Y. S.; Watanabe, K.; Taniguchi, T.; Kim, J.; et al. Electrically driven strain-induced deterministic single-photon emitters in a van der Waals heterostructure. *Sci. Adv.* **2021**, *7* (43), No. eabj3176.

(14) Terrones, M.; Botello-Méndez, A. R.; Campos-Delgado, J.; López-Urías, F.; Vega-Cantú, Y. I.; Rodríguez-Macías, F. J.; Elías, A. L.; Muñoz-Sandoval, E.; Cano-Márquez, A. G.; Charlier, J.-C.; et al. Graphene and graphite nanoribbons: Morphology, properties, synthesis, defects and applications. *Nano Today* **2010**, *5* (4), 351−372.

(15) Chowdhury, T.; Kim, J.; Sadler, E. C.; Li, C.; Lee, S. W.; Jo, K.; Xu, W.; Gracias, D. H.; Drichko, N. V.; Jariwala, D. Substrate-directed synthesis of MoS_2 nanocrystals with tunable dimensionality and optical properties. *Nat. Nanotechnol.* **2020**, *15* (1), 29−34.

(16) Li, S. S.; Lin, Y. C.; Zhao, W.; Wu, J.; Wang, Z.; Hu, Z. H.; Shen, Y. D.; Tang, D. M.; Wang, J. Y.; Zhang, Q.; et al. Vapour-liquid-solid growth of monolayer MoS_2 nanoribbons. *Nat. Mater.* **2018**, *17* (6), 535−542.

(17) Xu, H.; Liu, S. L.; Ding, Z. J.; Tan, S. J. R.; Yam, K. M.; Bao, Y.; Nai, C. T.; Ng, M. F.; Lu, J.; Zhang, C.; et al. Oscillating edge states in one-dimensional MoS_2 nanowires. *Nat. Commun.* **2016**, *7*, 12904.

(18) Aljarb, A.; Fu, J. H.; Hsu, C. C.; Chuu, C. P.; Wan, Y.; Hakami, M.; Naphade, D. R.; Yengel, E.; Lee, C. J.; Brems, S.; et al. Ledge-directed epitaxy of continuously self-aligned single-crystalline nanoribbons of transition metal dichalcogenides. *Nat. Mater.* **2020**, *19* (12), 1300−1306.

(19) Guo, J.; Xiang, R.; Cheng, T.; Maruyama, S.; Li, Y. One-Dimensional van der Waals Heterostructures: A Perspective. *ACS Nanosci. Au* **2022**, *2* (1), 3−11.

(20) Xiang, R.; Inoue, T.; Zheng, Y.; Kumamoto, A.; Qian, Y.; Sato, Y.; Liu, M.; Tang, D.; Gokhale, D.; Guo, J.; et al. One-dimensional van der Waals heterostructures. *Science* **2020**, *367* (6477), 537−542.

(21) Balandin, A. A.; Kargar, F.; Salguero, T. T.; Lake, R. K. One-dimensional van der Waals quantum materials. *Mater. Today* **2022**, *55*, 74−91.

(22) Liu, G. X.; Rumyantsev, S.; Bloodgood, M. A.; Salguero, T. T.; Shur, M.; Balandin, A. A. Low-Frequency Electronic Noise in Quasi-1D $TaSe_3$ van der Waals Nanowires. *Nano Lett.* **2017**, *17* (1), 377−383.

(23) Formo, E. V.; Hachtel, J. A.; Ghafouri, Y.; Bloodgood, M. A.; Salguero, T. T. Thermal Stability of Quasi-1D NbS_3 Nanoribbons and Their Transformation to 2D NbS_2: Insights from in Situ Electron Microscopy and Spectroscopy. *Chem. Mater.* **2022**, *34* (1), 279−287.

(24) Pfister, D.; Schäfer, K.; Ott, C.; Gerke, B.; Pöttgen, R.; Janka, O.; Baumgartner, M.; Efimova, A.; Hohmann, A.; Schmidt, P. Inorganic double helices in semiconducting SnIP. *Adv. Mater.* **2016**, *28* (44), 9783−9791.

(25) Farley, K. E.; Shi, Z.; Sambandamurthy, G.; Banerjee, S. Charge density waves in individual nanoribbons of orthorhombic-TaS_3. *Phys. Chem. Chem. Phys.* **2015**, *17* (28), 18374−18379.

(26) Autes, G.; Isaeva, A.; Moreschini, L.; Johannsen, J. C.; Pisoni, A.; Mori, R.; Zhang, W. T.; Filatova, T. G.; Kuznetsov, A. N.; Forro, L.; et al. A novel quasi-one-dimensional topological insulator in bismuth iodide β-Bi_4I_4. *Nat. Mater.* **2016**, *15* (2), 154−158.

(27) Qu, Y.; Arguilla, M. Q.; Zhang, Q.; He, X.; Dinca, M. Ultrathin, High-Aspect Ratio, and Free-Standing Magnetic Nanowires by Exfoliation of Ferromagnetic Quasi-One-Dimensional van der Waals Lattices. *J. Am. Chem. Soc.* **2021**, *143* (46), 19551−19558.

(28) Noguchi, R.; Kobayashi, M.; Jiang, Z. Z.; Kuroda, K.; Takahashi, T.; Xu, Z. F.; Lee, D.; Hirayama, M.; Ochi, M.; Shirasawa, T.; et al. Evidence for a higher-order topological insulator in a three-dimensional material built from van der Waals stacking of bismuth-halide chains. *Nat. Mater.* **2021**, *20* (4), 473−479.

(29) Fu, B.; Wang, H. W.; Shen, S. Q. Dirac Polarons and Resistivity Anomaly in $ZrTe_5$ and $HfTe_5$. *Phys. Rev. Lett.* **2020**, *125* (25), No. 256601.

(30) Lu, Y.; Kono, H.; Larkin, T.; Rost, A.; Takayama, T.; Boris, A.; Keimer, B.; Takagi, H. Zero-gap semiconductor to excitonic insulator transition in Ta_2NiSe_5. *Nat. Commun.* **2017**, *8* (1), 14408.

(31) Lin, C.; Ochi, M.; Noguchi, R.; Kuroda, K.; Sakoda, M.; Nomura, A.; Tsubota, M.; Zhang, P.; Bareille, C.; Kurokawa, K. Visualization of the strain-induced topological phase transition in a quasi-one-dimensional superconductor $TaSe_3$. *Nat. Mater.* **2021**, *20* (8), 1093−1099.

https://doi.org/10.1021/acs.chemmater.3c02114
Chem. Mater. 2024, 36, 730−741

(32) Yue, B. B.; Zhong, W.; Deng, W.; Wen, T.; Wang, Y. G.; Yin, Y. Y.; Shan, P. F.; Wang, J. T.; Yu, X. H.; Hong, F. Insulator-to-Superconductor Transition in Quasi-One-Dimensional HfS_3 under Pressure. *J. Am. Chem. Soc.* **2023**, *145* (2), 1301−1309.
(33) Fan, L.; Huang, D.; Wang, Y.; Miao, Z.; Ma, Y.; Zhao, Q.; Zha, Z. Cryo-assisted exfoliation of atomically thin 2D Sb_2Se_3 nanosheets for photo-induced theranostics. *Chem. Commun.* **2019**, *55* (19), 2805−2808.
(34) Lipatov, A.; Loes, M. J.; Lu, H. D.; Dai, J.; Patoka, P.; Vorobeva, N. S.; Muratov, D. S.; Ulrich, G.; Kastner, B.; Hoehl, A.; et al. Quasi-1D TiS_3 Nanoribbons: Mechanical Exfoliation and Thickness-Dependent Raman Spectroscopy. *ACS Nano* **2018**, *12* (12), 12713−12720.
(35) Song, H.; Li, T.; Zhang, J.; Zhou, Y.; Luo, J.; Chen, C.; Yang, B.; Ge, C.; Wu, Y.; Tang, J. Highly anisotropic Sb_2Se_3 nanosheets: gentle exfoliation from the bulk precursors possessing 1D crystal structure. *Adv. Mater.* **2017**, *29* (29), No. 1700441.
(36) Tan, S. M.; Mayorga-Martinez, C. C.; Sofer, Z.; Pumera, M. Bipolar electrochemistry exfoliation of layered metal chalcogenides Sb_2S_3 and Bi_2S_3 and their hydrogen evolution applications. *Chem. − Eur. J.* **2020**, *26* (29), 6479−6483.
(37) Don, C. H.; Shiel, H.; Hobson, T. D.; Savory, C. N.; Swallow, J. E.; Smiles, M. J.; Jones, L. A.; Featherstone, T. J.; Thakur, P. K.; Lee, T.-L. Sb $5s^2$ lone pairs and band alignment of Sb_2Se_3: a photoemission and density functional theory study. *J. Mater. Chem. C* **2020**, *8* (36), 12615−12622.
(38) Wang, X.; Li, Z.; Kavanagh, S. R.; Ganose, A. M.; Walsh, A. Lone pair driven anisotropy in antimony chalcogenide semiconductors. *Phys. Chem. Chem. Phys.* **2022**, *24* (12), 7195−7202.
(39) Wang, M.; Xu, X. W.; Ge, Y. C.; Dong, P.; Baines, R.; Ajayan, P. M.; Ye, M. X.; Shen, J. F. Surface Tension Components Ratio: An Efficient Parameter for Direct Liquid Phase Exfoliation. *ACS Appl. Mater. Interfaces* **2017**, *9* (10), 9168−9175.
(40) Voutsas, G. P.; Papazoglou, A. G.; Rentzeperis, P. J. The crystal structure of antimony selenide, Sb_2Se_3. *Z. Kristallogr. Cryst. Mater.* **1985**, *171* (3−4), 261−268.
(41) Bayliss, P.; Nowacki, W. Refinement of Crystal Structure of Stibnite, Sb_2S_3. *Z. Kristallogr. Cryst. Mater.* **1972**, *135* (3−4), 308−315.
(42) Caruso, F.; Filip, M. R.; Giustino, F. Excitons in one-dimensional van der Waals materials: Sb_2S_3 nanoribbons. *Phys. Rev. B* **2015**, *92* (12), No. 125134.
(43) Peng, Y.; Xia, C.; Tan, Z.; An, J.; Zhang, Q. Size-controlled excitonic effects on electronic and optical properties of Sb_2S_3 nanowires. *Phys. Chem. Chem. Phys.* **2019**, *21* (48), 26515−26524.
(44) Chen, C.; Bobela, D. C.; Yang, Y.; Lu, S.; Zeng, K.; Ge, C.; Yang, B.; Gao, L.; Zhao, Y.; Beard, M. C.; et al. Characterization of basic physical properties of Sb_2Se_3 and its relevance for photovoltaics. *Front. Optoelectron.* **2017**, *10* (1), 18−30.
(45) Chen, C.; Li, K.; Tang, J. Ten Years of Sb_2Se_3 Thin Film Solar Cells. *Sol. RRL* **2022**, *6* (7), No. 2200094.
(46) Delaney, M.; Zeimpekis, I.; Du, H.; Yan, X.; Banakar, M.; Thomson, D. J.; Hewak, D. W.; Muskens, O. L. Nonvolatile programmable silicon photonics using an ultralow-loss Sb_2Se_3 phase change material. *Sci. Adv.* **2021**, *7* (25), No. eabg3500.
(47) Ma, Z.; Chai, S.; Feng, Q.; Li, L.; Li, X.; Huang, L.; Liu, D.; Sun, J.; Jiang, R.; Zhai, T. Chemical vapor deposition growth of high crystallinity Sb_2Se_3 nanowire with strong anisotropy for near-infrared photodetectors. *Small* **2019**, *15* (9), No. 1805307.
(48) Mavlonov, A.; Razykov, T.; Raziq, F.; Gan, J.; Chantana, J.; Kawano, Y.; Nishimura, T.; Wei, H.; Zakutayev, A.; Minemoto, T.; et al. A review of Sb_2Se_3 photovoltaic absorber materials and thin-film solar cells. *Sol. Energy* **2020**, *201*, 227−246.
(49) Zhou, Y.; Wang, L.; Chen, S.; Qin, S.; Liu, X.; Chen, J.; Xue, D.-J.; Luo, M.; Cao, Y.; Cheng, Y. Thin-film Sb_2Se_3 photovoltaics with oriented one-dimensional ribbons and benign grain boundaries. *Nat. Photonics* **2015**, *9* (6), 409−415.
(50) Li, J.; Niu, Y.; Zeng, J.; Wang, J.; Wang, Q.; Liu, X.; Li, H.; de Rooij, N. F.; Wang, Y.; Zhou, G. Electrochemical Exfoliation of Naturally Occurring Layered Mineral Stibnite (Sb_2S_3) for Highly Sensitive and Fast Room-Temperature Acetone Sensing. *Adv. Mater. Interfaces* **2022**, *9* (19), No. 2200605.
(51) Carey, J. J.; Allen, J. P.; Scanlon, D. O.; Watson, G. W. The electronic structure of the antimony chalcogenide series: Prospects for optoelectronic applications. *J. Solid State Chem.* **2014**, *213*, 116−125.
(52) Cain, J. D.; Oh, S.; Azizi, A.; Stonemeyer, S.; Dogan, M.; Thiel, M.; Ercius, P.; Cohen, M. L.; Zettl, A. Ultranarrow TaS_2 Nanoribbons. *Nano Lett.* **2021**, *21* (7), 3211−3217.
(53) Pham, T.; Oh, S.; Stetz, P.; Onishi, S.; Kisielowski, C.; Cohen, M. L.; Zettl, A. Torsional instability in the single-chain limit of a transition metal trichalcogenide. *Science* **2018**, *361* (6399), 263−266.
(54) Stonemeyer, S.; Cain, J. D.; Oh, S.; Azizi, A.; Elasha, M.; Thiel, M.; Song, C.; Ercius, P.; Cohen, M. L.; Zettl, A. Stabilization of $NbTe_3$, VTe_3, and $TiTe_3$ via Nanotube Encapsulation. *J. Am. Chem. Soc.* **2021**, *143* (12), 4563−4568.
(55) Gao, M.; Park, Y.; Jin, J.; Chen, P.-C.; Devyldere, H.; Yang, Y.; Song, C.; Lin, Z.; Zhao, Q.; Siron, M.; et al. Direct Observation of Transient Structural Dynamics of Atomically Thin Halide Perovskite Nanowires. *J. Am. Chem. Soc.* **2023**, *145* (8), 4800−4807.
(56) Hu, Z.; Breeze, B.; Kashtiban, R. J.; Sloan, J.; Lloyd-Hughes, J. Zigzag HgTe Nanowires Modify the Electron−Phonon Interaction in Chirality-Refined Single-Walled Carbon Nanotubes. *ACS Nano* **2022**, *16* (4), 6789−6800.
(57) Hu, Z.; Breeze, B.; Walker, M.; Faulques, E.; Sloan, J.; Lloyd-Hughes, J. Spectroscopic Insights into the Influence of Filling Carbon Nanotubes with Atomic Nanowires for Photophysical and Photochemical Applications. *ACS Appl. Nano Mater.* **2023**, *6* (4), 2883−2893.
(58) Kashtiban, R. J.; Burdanova, M. G.; Vasylenko, A.; Wynn, J.; Medeiros, P. V. C.; Ramasse, Q.; Morris, A. J.; Quigley, D.; Lloyd-Hughes, J.; Sloan, J. Linear and Helical Cesium Iodide Atomic Chains in Ultranarrow Single-Walled Carbon Nanotubes: Impact on Optical Properties. *ACS Nano* **2021**, *15* (8), 13389−13398.
(59) Kashtiban, R. J.; Patrick, C. E.; Ramasse, Q.; Walton, R. I.; Sloan, J. Picoperovskites: The Smallest Conceivable Isolated Halide Perovskite Structures Formed within Carbon Nanotubes. *Adv. Mater.* **2023**, *35* (10), No. 2208575.
(60) Slade, C. A.; Sanchez, A. M.; Sloan, J. Unprecedented New Crystalline Forms of SnSe in Narrow to Medium Diameter Carbon Nanotubes. *Nano Lett.* **2019**, *19* (5), 2979−2984.
(61) Sloan, J.; Wright, D. M.; Bailey, S.; Brown, G.; York, A. P. E.; Coleman, K. S.; Green, M. L. H.; Sloan, J.; Wright, D. M.; Hutchison, J. L.; et al. Capillarity and silver nanowire formation observed in single walled carbon nanotubes. *Chem. Commun.* **1999**, *8*, 699−700.
(62) Spencer, J. H.; Nesbitt, J. M.; Trewhitt, H.; Kashtiban, R. J.; Bell, G.; Ivanov, V. G.; Faulques, E.; Sloan, J.; Smith, D. C. Raman Spectroscopy of Optical Transitions and Vibrational Energies of ∼ 1 nm HgTe Extreme Nanowires within Single Walled Carbon Nanotubes. *ACS Nano* **2014**, *8* (9), 9044−9052.
(63) Ajayan, P.; Ebbesen, T.; Ichihashi, T.; Iijima, S.; Tanigaki, K.; Hiura, H. Opening carbon nanotubes with oxygen and implications for filling. *Nature* **1993**, *362*, 522−525.
(64) Ajayan, P. M.; Lijima, S. Capillarity-induced filling of carbon nanotubes. *Nature* **1993**, *361* (6410), 333−334.
(65) Fujimori, T.; Morelos-Gómez, A.; Zhu, Z.; Muramatsu, H.; Futamura, R.; Urita, K.; Terrones, M.; Hayashi, T.; Endo, M.; Young Hong, S.; et al. Conducting linear chains of sulphur inside carbon nanotubes. *Nat. Commun.* **2013**, *4* (1), 2162.
(66) Medeiros, P. V. C.; Marks, S.; Wynn, J. M.; Vasylenko, A.; Ramasse, Q. M.; Quigley, D.; Sloan, J.; Morris, A. J. Single-Atom Scale Structural Selectivity in Te Nanowires Encapsulated Inside Ultranarrow. *Single-Walled Carbon Nanotubes. ACS Nano* **2017**, *11* (6), 6178−6185.
(67) Stonemeyer, S.; Dogan, M.; Cain, J. D.; Azizi, A.; Popple, D. C.; Culp, A.; Song, C.; Ercius, P.; Cohen, M. L.; Zettl, A. Targeting One- and Two-Dimensional Ta−Te Structures via Nanotube Encapsulation. *Nano Lett.* **2022**, *22* (6), 2285−2292.

(68) Krichevsky, D. M.; Shi, L.; Baturin, V. S.; Rybkovsky, D. V.; Wu, Y.; Fedotov, P. V.; Obraztsova, E. D.; Kapralov, P. O.; Shilina, P. V.; Fung, K.; et al. Magnetic nanoribbons with embedded cobalt grown inside single-walled carbon nanotubes. *Nanoscale* **2022**, *14* (5), 1978−1989.
(69) Hanwell, M. D.; Curtis, D. E.; Lonie, D. C.; Vandermeersch, T.; Zurek, E.; Hutchison, G. R. Avogadro: an advanced semantic chemical editor, visualization, and analysis platform. *J. Cheminf.* **2012**, *4* (1), 1−17.
(70) Momma, K.; Izumi, F. VESTA 3 for three-dimensional visualization of crystal, volumetric and morphology data. *J. Appl. Crystallogr.* **2011**, *44* (6), 1272−1276.
(71) Peters, J. J. P. A Fast Frozen Phonon Algorithm Using Mixed Static Potentials. *Ultramicroscopy* **2021**, *229*, No. 113364.
(72) Duncan, D. R. The colour of pigment mixtures. *Proc. Phys. Soc. London* **1940**, *52* (3), 390.
(73) Clark, S. J.; Segall, M. D.; Pickard, C. J.; Hasnip, P. J.; Probert, M. I.; Refson, K.; Payne, M. C. First principles methods using CASTEP. *Zeitschrift für kristallographie-crystalline materials* **2005**, *220* (5−6), 567−570.
(74) Perdew, J. P.; Burke, K.; Ernzerhof, M. Generalized gradient approximation made simple. *Phys. Rev. Lett.* **1996**, *77* (18), 3865.
(75) Grimme, S. Semiempirical GGA-type density functional constructed with a long-range dispersion correction. *J. Comput. Chem.* **2006**, *27* (15), 1787−1799.
(76) Tang, W.; Sanville, E.; Henkelman, G. A grid-based Bader analysis algorithm without lattice bias. *J. Phys.: Condens. Matter* **2009**, *21* (8), No. 084204.
(77) Sanville, E.; Kenny, S. D.; Smith, R.; Henkelman, G. Improved grid-based algorithm for Bader charge allocation. *J. Comput. Chem.* **2007**, *28* (5), 899−908.
(78) Ghosh, G. The Sb-Se (antimony-selenium) system. *Journal of phase equilibria* **1993**, *14* (6), 753−763.
(79) Shen, K.; Zhang, Y.; Wang, X.; Ou, C.; Guo, F.; Zhu, H.; Liu, C.; Gao, Y.; Schropp, R. E.; Li, Z. Efficient and stable planar n−i−p Sb_2Se_3 solar cells enabled by oriented 1D trigonal selenium structures. *Adv. Sci.* **2020**, *7* (16), No. 2001013.
(80) Dresselhaus, M. S.; Dresselhaus, G.; Saito, R.; Jorio, A. Raman spectroscopy of carbon nanotubes. *Physics reports* **2005**, *409* (2), 47−99.
(81) Vidal-Fuentes, P.; Guc, M.; Alcobe, X.; Jawhari, T.; Placidi, M.; Pérez-Rodríguez, A.; Saucedo, E.; Roca, V. I. Multiwavelength excitation Raman scattering study of Sb_2Se_3 compound: fundamental vibrational properties and secondary phases detection. *2D Mater.* **2019**, *6* (4), No. 045054.
(82) Fleck, N.; Hobson, T. D.; Savory, C. N.; Buckeridge, J.; Veal, T. D.; Correia, M. R.; Scanlon, D. O.; Durose, K.; Jäckel, F. Identifying Raman modes of Sb_2Se_3 and their symmetries using angle-resolved polarised Raman spectra. *J. Mater. Chem. A* **2020**, *8* (17), 8337−8344.
(83) Son, Y.-R.; Park, S.-J. Green preparation and characterization of graphene oxide/carbon nanotubes-loaded carboxymethyl cellulose nanocomposites. *Sci. Rep.* **2018**, *8* (1), 17601.
(84) Filip, M. R.; Patrick, C. E.; Giustino, F. GW quasiparticle band structures of stibnite, antimonselite, bismuthinite, and guanajuatite. *Phys. Rev. B* **2013**, *87* (20), No. 205125.
(85) Vadapoo, R.; Krishnan, S.; Yilmaz, H.; Marin, C. Orientation dependence of electronic properties of antimony selenide nanowires. *Nano Express* **2022**, *3* (3), No. 035008.
(86) Cordova, D. L. M.; Chua, K.; Huynh, R. M.; Aoki, T.; Arguilla, M. Q. Anisotropy-Driven Crystallization of Dimensionally Resolved Quasi-1D Van der Waals Nanostructures. *J. Am. Chem. Soc.* **2023**, *145* (41), 22413−22424.
(87) Karguppikar, A.; Vedeshwar, A. Thickness dependence of the forbidden energy gap in stibnite (Sb2S3) thin films. *Phys. Lett. A* **1987**, *126* (2), 123−126.
(88) Clark, S. J.; Segall, M. D.; Pickard, C. J.; Hasnip, P. J.; Probert, M. I.; Refson, K.; Payne, M. C. First principles methods using CASTEP. *Z. Kristallogr. Cryst. Mater.* **2005**, *220* (5−6), 567−570.
(89) Matsuda, Y.; Tahir-Kheli, J.; Goddard, W. A., III Definitive band gaps for single-wall carbon nanotubes. *J. Phys. Chem. Lett.* **2010**, *1* (19), 2946−2950.
(90) Dresselhaus, M.; Dresselhaus, G.; Saito, R. Physics of carbon nanotubes. *Carbon* **1995**, *33* (7), 883−891.
(91) Saito, R.; Fujita, M.; Dresselhaus, G.; Dresselhaus, U. M. Electronic structure of chiral graphene tubules. *Appl. Phys. Lett.* **1992**, *60* (18), 2204−2206.
(92) Vasylenko, A.; Marks, S.; Wynn, J. M.; Medeiros, P. V.; Ramasse, Q. M.; Morris, A. J.; Sloan, J.; Quigley, D. Electronic structure control of sub-nanometer 1D SnTe via nanostructuring within single-walled carbon nanotubes. *ACS Nano* **2018**, *12* (6), 6023−6031.
(93) Fujimori, T.; dos Santos, R. B.; Hayashi, T.; Endo, M.; Kaneko, K.; Tománek, D. Formation and properties of selenium double-helices inside double-wall carbon nanotubes: experiment and theory. *ACS Nano* **2013**, *7* (6), 5607−5613.
(94) Fujimori, T.; Morelos-Gómez, A.; Zhu, Z.; Muramatsu, H.; Futamura, R.; Urita, K.; Terrones, M.; Hayashi, T.; Endo, M.; Young Hong, S. Conducting linear chains of sulphur inside carbon nanotubes. *Nat. Commun.* **2013**, *4* (1), 2162.
(95) Komsa, H.-P.; Senga, R.; Suenaga, K.; Krasheninnikov, A. V. Structural distortions and charge density waves in iodine chains encapsulated inside carbon nanotubes. *Nano Lett.* **2017**, *17* (6), 3694−3700.

https://doi.org/10.1021/acs.chemmater.3c02114
Chem. Mater. 2024, 36, 730−741